Journal of Materials Chemistry C

ROYAL SOCIETY OF CHEMISTRY

PAPER

View Article Online
View Journal

Cite this: DOI: 10.1039/d5tc04261e

Deciphering multiple energy-transfer photoevents in a 2D-MOF composite: relevance to multicolor lighting

Samita Mishra, [a] Jordi Torró-Abril, [b] Urbano Díaz, [b] Boiko Cohen *[a] and Abderrazzak Douhal *[a]

Received 3rd December 2025,
Accepted 23rd March 2026

DOI: 10.1039/d5tc04261e

rsc.li/materials-c

Incorporating different emitters within metal–organic frameworks (MOFs) allows tunable emission colors *via* energy transfer (ET) for desired and colorful lighting. Here in, we report on multiple dyes interacting with 2D hybrid MOF composed of Al clusters and 4-heptylbenzoic acid (HB) linkers (Al-ITQ-HB) exhibiting efficient ET from Coumarin 153 (C153) to Nile red (NR) and a broad emission spectrum. The C153@Al-ITQ-HB composites revealed emissions from adsorbed locally excited (0.15–0.25 ns), charge-separated (1.1–2.4 ns), and J-aggregates (3.4–5.7 ns) of C153 species along with a relatively fast homo-ET process (0.2–0.4 ns). However, in the C153/NR@Al-ITQ-HB composites, while the dual emission and time constant of the hetero-ET from C153 to NR weakly depend on C153 concentration, the photobehaviour strongly depends on the NR one and the hetero-ET times are longer (1.1–2.5 ns). Fluorescence lifetime imaging microscopy on single crystals shows homogeneous dye distribution within each crystal but different dye loading across different crystals of the same batch. These results highlight the impact of the donor–acceptor concentrations on ET within composites of two emitters, enabling tunable dual emissions for possible applications in lighting and optoelectronic devices.

1. Introduction

Although quantum dots (QDs), perovskites, and other nanomaterials have emerged as promising materials in solar cells, light-emitting diodes (LEDs), and bioimaging, largely due to their exceptional optical and electronic properties, the organic chromophores continue to hold a vital place in photonics applications.[1,2] They serve as key building blocks in the development of new materials and are fundamental to optoelectronic systems including displays, sensors, OLEDs, and biomedical imaging platforms.[3–7] Their advantages, including cost-effectiveness and tunable emission, make them compelling alternatives to conventional rare-earth-based luminescent materials and other nano/micro materials.[8–11] A main drawback in their use is the tendency to form aggregates, a process that may alter their emission properties. It can lead to either aggregation-induced emission (AIE) or aggregation-caused quenching (ACQ). While AIE opens new possibilities for photonics applications, ACQ limits their practical use in solid-state optoelectronic devices.[12–15] To avoid ACQ, supramolecular encapsulation is a promising strategy that separates the dye molecules and inhibits self-aggregation or other comparable interactions.[16–18]

Metal organic frameworks (MOFs), a type of porous coordination polymers made by organic linkers and metal clusters, have emerged as potential hosts for different types of chromophores due to their structural versatility, high porosity, and ability to encapsulate guest molecules.[19–28] Additionally, they have high surface area, tunable pore sizes and can be functionalized, allowing for precise control over their luminescent properties.[29,30] MOFs can encapsulate organic dyes, metal complexes, and other emissive species, providing a versatile platform for energy transfer (ET) and spectral tuning.[31,32] The ET mechanisms in MOFs are particularly interesting for white light (WL) generation.[33] Energy can be transferred from the fluorescent MOF to the encapsulated dye or metal complex, or *vice versa*, depending on the design of the system.[34,35] An alternative approach involves encapsulation of multiple guest molecules within 3D MOF structures, enabling cascade ET to generate WL.[36,37] However, due to the inherent structural characteristics of the 3D MOFs, the direct interaction between the encapsulated dyes and the spatial orientation required for such interactions are restricted.

[a] *Departamento de Química Física, Facultad de Ciencias Ambientales y Bioquímica, and INAMOL, Universidad de Castilla-La Mancha, Avenida Carlos III, S/N, 45071 Toledo, Spain. E-mail: Abderrazzak.Douhal@uclm.es, Boiko.Cohen@uclm.es; Tel: +34-925-265717*

[b] *Instituto de Tecnología Química, Universitat Politecnica de ValenciaConsejo Superior de Investigaciones Científicas (UPV-CSIC), Avenida de los Naranjos s/n, 46022 Valencia, Spain*

As an alternative to the 3D MOFs, the distinctive features of 2D MOFs, such as multiple exposed active sites and nanoscale dimensions, have attracted significant interest. MOF nanosheets can be used in a variety of fields, including energy storage, light harvesting, catalysis, and sensing. It has been demonstrated that 2D MOFs are more effective than their analogous 3D or 0D materials for dye adsorption and catalytic applications.[38] Compared to the bulk MOFs, the ultrathin MOF nanosheets may mitigate scattering and nonuniform backlight absorption.[39] A distinct class of 2D MOFs, referred to as Al-ITQ-R, has been developed using aluminum (Al) as the metal center and alkyl-substituted benzoic acids as organic spacers. Here, "R" denotes the specific alkyl group attached at the para-position of the benzoic acid ring, with the following variants: 4-ethylbenzoic acid (EB), 4-heptylbenzoic acid (HB), and 4-dodecylbenzoic acid (DB).[40] Al-ITQ-HB is an example of a 2D MOF with a structure formed by aluminum clusters coordinated with HB ligands.[41,42] Previous research on Al-ITQ-HB 2D-MOF has explored its interaction with NR and *trans*-4-(dicyanomethylene)-2-methyl-6-(4-dimethylaminostyryl)-4*H*-pyran (DCM), demonstrating the presence of different emitting populations and tunable emission behavior.[41,43–45] It was shown that the MOF framework not only provides a protective environment that reduces ACQ but also influences the emission wavelength and intensity of the interacting chromophore through environmental effects.[46,47] While the photodynamics of single dyes have been previously reported, study of multiple chromophores within 2D Al-ITQ-HB remains unexplored. The presence of different largely emitting guests within this 2D-MOF will allow getting a broad and intense emission that might be tunable through a control of the relative concentration of the trapped guests in the composite.

In this work, we report on the adsorption and emission behavior of C153 and NR adsorbed on Al-ITQ-HB (Scheme 1) and analyze the impact of their relative concentrations on the efficiency of the ET process and the photophysical properties of the formed composites. We first explored the effect of different initial concentrations of C153 in the C153@Al-ITQ-HB composites. The steady-state and time-resolved emission experiments show that the emission arises from adsorbed monomers (locally excited and charge-separated states), H- and J-aggregates of adsorbed C153. Homo-ET at higher dye concentrations in the composites occurs with a time constant of 0.2–0.4 ns. For the C153/NR@Al-ITQ-HB composites, the ET from C153 to NR and the resulting emission are mainly affected by the initial concentration of the energy-acceptor dye (NR). We observed both C153–C153 homo- and C153-NR hereto-ET. At higher initial concentration of NR (10^{-4} M), the hetero-ET occurs in ~1.1 ns and the resulting emission mainly corresponds to NR. However, at lower initial concentrations of NR (10^{-5} M) the hetero-ET occurs in ~2.5 ns, but the resulting emission has the signature of both adsorbed dyes. Single-crystal emission studies suggest different dyes content in different crystals of the same synthesized sample, but a homogeneous dye distribution within each crystal. The results provide new insights into the dynamics and spectroscopy of multiple ET processes for efficient and dual emission from 2D MOF-based composites that adsorb two different emitters for applications in various optical materials.

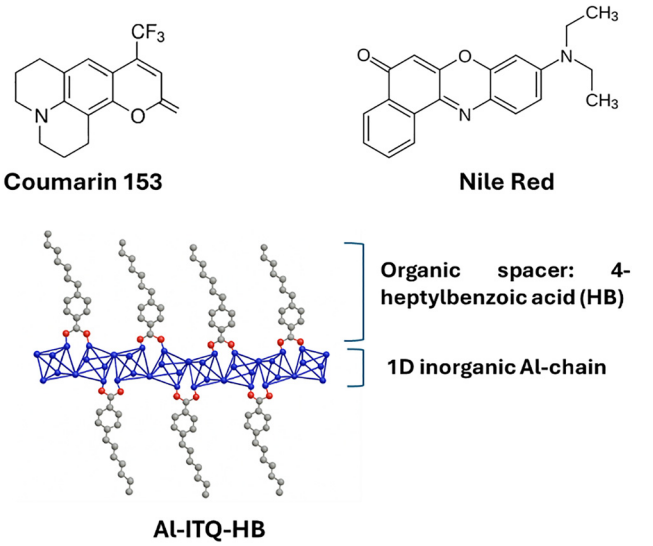

Scheme 1 Molecular structure of coumarin 153 (C153), Nile red (NR) dyes and schematic presentation of Al-ITQ-HB 2D MOF. The Al-ITQ-HB is shown as individual organic–inorganic nanosheet. Individual nanosheets are formed by 1D chains by consecutive corner-sharing octahedral (AlO_6) units, separated by alkyl benzene monocarboxylate ligands, located on both sides of metallic nodes.[41]

2. Experimental section

Detailed information of the synthetic procedure for Al-ITQ-HB is provided in the SI along with a description of the preparation of C153@Al-ITQ-HB and C153/NR@Al-ITQ-HB composites. Further details on the methods and techniques used for structural and spectroscopic characterization are provided in the SI. The photophysical properties of the composites were characterized by a combination of complementary spectroscopic techniques, including steady-state absorption and emission, time-correlated single-photon counting and fluorescence microscopy systems. We did not observe any effect on the dye loading preparation method on the photophysical properties of the studied composites.

3. Results and discussion

3.1. Steady-state spectra of C153@Al-ITQ-HB MOF

To begin with the C153 interacting with Al-ITQ-HB, we recorded the steady-state behavior of the C153@Al-ITQ-HB composites in solid state. The absorption spectrum of Al-ITQ-HB in solid state has been reported previously.[44] Fig. 1A shows the normalized UV-vis absorption and emission spectra of the composites having five different initial concentrations of C153 ($[C153]_0$: 10^{-6}, 10^{-5}, 10^{-4}, 10^{-3}, and 10^{-2} M). While the solid amorphous dye exhibits an absorption maximum at 425 nm with a full-width at half-maximum (FWHM) intensity of ~5140 cm^{-1}, the absorption band for the C153@Al-ITQ-HB composites is

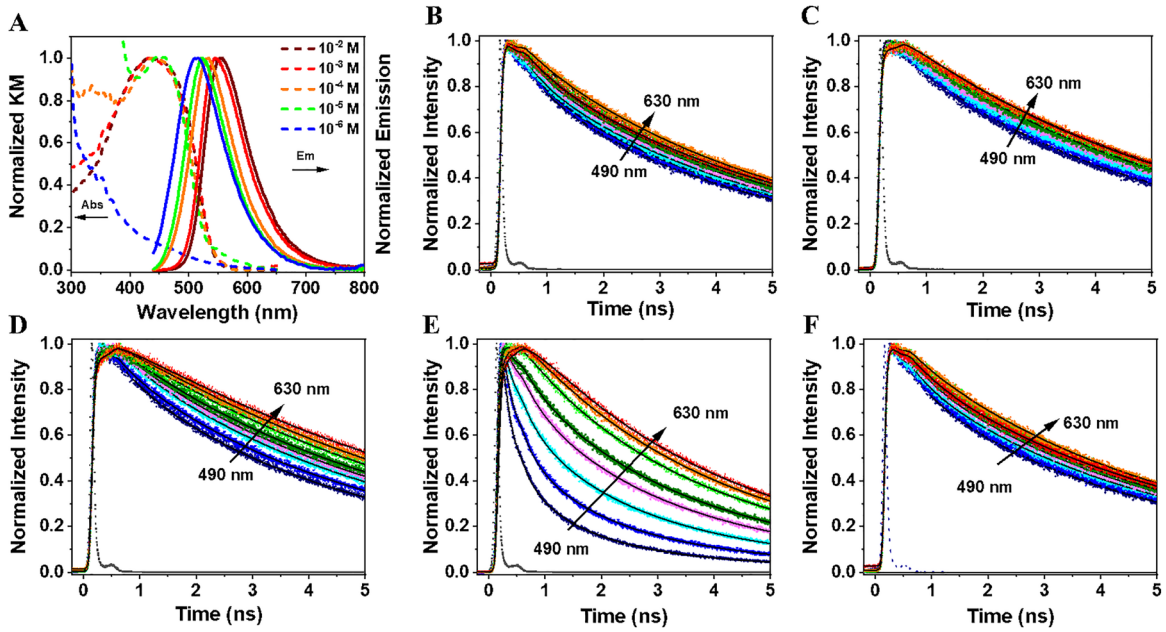

Fig. 1 (A) UV-vis absorption (dashed lines) and emission spectra (solid lines, λ_{ex} = 425 nm) of C153@Al-ITQ-HB composites with different $[C153]_0$: 10^{-6} M (blue), 10^{-5} M (green), 10^{-4} M (orange); 10^{-3} M (red) and 10^{-2} M (brown); (B)–(F) Emission decays (solid circles) of C153@Al-ITQ-HB composites at different wavelengths of observation (490, 500, 510, 520, 530, 560, 590 and 630 nm) upon excitation at 433 nm. The solid lines (black) represent the multiexponential fit of the decays. The dashed line is the instrument response function (IRF ~ 70 ps). The used dye concentrations in C153@Al-ITQ-HB composites for the decays are: (B) 10^{-6}, (C) 10^{-5}, (D) 10^{-4}, (E) 10^{-3} and (F) 10^{-2} M.

significantly broader and red-shifted (Fig. S2A). The UV-vis absorption spectrum of the composites made with 10^{-6} M $[C153]_0$ shows a broad and structureless band throughout the visible region, with no prominent peak corresponding to C153. The 10^{-5} M $[C153]_0$ composite also exhibits a broad absorption, but with the maximum intensity at 453 nm and a FWHM ~5590 cm^{-1}. The composites with higher $[C153]_0$: 10^{-4}, 10^{-3} and 10^{-2} M, show broad and structureless bands with the maximum absorption intensity at 448, 446 and 440 nm with FWHM of ~6450, ~9210 and 9410 cm^{-1}, respectively. The spectral behavior of the composites indicates the interaction between C153 and the Al-ITQ-HB framework, as well as the presence of several populations arising from different C153–C153 and C153–MOF interactions. Because of the layered structure of the 2D Al-ITQ-HB, we suggest that adsorbed C153 molecules adopt various orientations on different sites of the MOF.[44,45]

To evaluate the photophysical behavior of the C153@Al-ITQ-HB composites, we compare their emission spectra with that of the pure solid C153 dye (Fig. S2B). Upon excitation at 425 nm, the emission spectrum of the solid C153 has the maximum emission intensity at 520 nm with a FWHM of ~1760 cm^{-1}. These spectra are different from those of a diluted solution of C153 (10^{-6} M) in dichloromethane where the maximum emission intensity is at 500 nm with and the FWHM is 3040 cm^{-1} (Fig. S2C). In the diluted solution, C153 exists primarily as monomer and does not form aggregates, resulting in a blue-shifted emission relative to the one of the solid C153, which tends to form aggregates, affecting its emission properties.

Upon excitation of the composites at 425 nm, we observed a concentration-dependent shift in the emission spectrum (Fig. 1A). At the lowest $[C153]_0$ (10^{-6} M), the emission is blue-shifted to 516 nm relative to the solid C153 dye (520 nm, Fig. S2B), indicating that the emission predominantly arises from monomeric C153 species. In contrast, for the higher used initial concentrations (10^{-4}, 10^{-3} and 10^{-2} M), the emission spectra display red-shifted peaks at 533, 546, and 556 nm, respectively, compared to the solid dye (520 nm). This red shift is attributed to increased dye aggregation at higher concentrations, which alters the local environment and promotes intermolecular interactions of the adsorbed C153 species. Interestingly, the 10^{-5} M $[C153]_0$ composite shows the highest emission intensity, with a peak position matching that of the solid C153 (Fig. S2B). Additionally, the emission band of the composites becomes significantly broader in comparison with that of the solid dye. The emission band of the 10^{-6} M $[C153]_0$ composite has a FWHM of ~3640 cm^{-1} that decreases upon increasing $[C153]_0$ and reaches 2730 cm^{-1} for the 10^{-2} M $[C153]_0$ composite. The broadening of the emission band of the C153@Al-ITQ-HB composites compared to the solid C153 indicates emission from different adsorbed populations on the Al-ITQ-HB surface, in agreement with previous studies on NR@Al-ITQ-HB composites prepared with different $[NR]_0$.[44,46,47] Table S1 gives a summary of the steady-state absorption and emission data of the C153 composites.

Fig. S3 shows the excitation spectra of the composites, recorded at the emission wavelength of the maximum intensity. For the 10^{-6} M $[C153]_0$ composites, the excitation spectrum exhibits a maximum intensity at 444 nm while for the 10^{-5} and

10^{-4} M $[C153]_0$ composites the maxima are at 439 and 435 nm, respectively, comparable to the respective absorption spectra. However, for the 10^{-2} M $[C153]_0$ composite, the maximum intensity is bathochrome-shifted when compared to the corresponding absorption ones, suggesting the existence of absorbing species that are not- or weakly-emissive, most likely due to aggregates with efficient ACQ. To explore this behavior, we recorded the emission decays.

3.2. Picosecond time-resolved behavior of C153@Al-ITQ-HB MOF

Thus, to elucidate the effect of $[C153]_0$ on the photodynamical properties of the composites, we conducted time-resolved studies with picosecond (ps) resolution (time-correlated single photon counting; TCSPC), exciting at 433 nm. Fig. 1B–F (up to 5 ns) and Fig. S4 (up to 25 ns) show the emission decays of the composites prepared using 5 different $[C153]_0$ of 10^{-6}, 10^{-5}, 10^{-4}, 10^{-3} and 10^{-2} M, recorded at different wavelengths. Fig. 1 (panels 1B and 1C) displays the emission decays of the composites with $[C153]_0$ = 10^{-6} and 10^{-5} M, while Table S2 and Table 1A, respectively, give the parameters obtained from the multi-exponential global fits. The decays exhibit a tri-exponential behavior with time constants of 0.25, 1.9, and 5.5 ns for 10^{-6} M $[C153]_0$, and 0.3, 2.4, and 5.7 ns for 10^{-5} M $[C153]_0$. The contributions of the shortest and intermediate components decrease, while that of the longest one increases with the observation wavelength. Upon tenfold increase in $[C153]_0$, the contributions of the short and intermediate components decrease while that of the longest one increases (Table 1A). We assign the shortest component to the relaxation of the locally excited (LE) state of surface adsorbed C153 monomers, while the intermediate component arises from the charge-separated (CS) state due to an intramolecular charge transfer (ICT) process in the C153 species. Finally, the longest component is from an aggregate-like population having suffered a fast homo-ET leading to a red-shifted emission (Scheme 2). The observed three components in the composites emission, originating from two distinct monomeric states (LE and CS), as well as from J-aggregates, are likely a result of C153 interacting with structurally and chemically diverse domains of Al-ITQ-HB with apolar and polar character providing distinct environments that influence their photobehavior.[27,42,44,46,47] We suggest that in the apolar domain, the C153 emission comes from the LE state, while in the more polar one it arises from its CS.[45–47] Polar environments promote dyes aggregation, consistent with the behavior of C153.[48] J-aggregates of C153 exhibit long lifetimes, and in our composites, the long emission component (~5.5 ns) is attributed to these aggregates. The longer component with less contribution in the blue region and more in the red one, again agrees with the emission character of J-aggregates.[48,49]

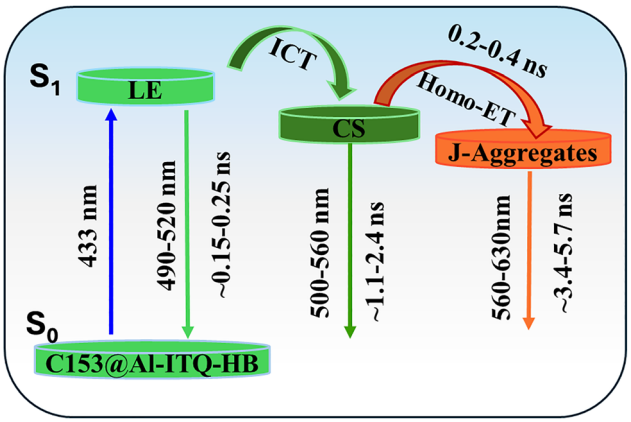

Scheme 2 Schematic presentation of the photophysical processes (not in scale) and the corresponding lifetime values giving information on spectral and dynamical behavior of the electronically first excited state of C153@Al-ITQ-HB. LE, ICT, ET, and CS correspond to locally excited state, intramolecular charge-transfer, energy-transfer and charge-separated state, respectively. The absorption and emission wavelengths are estimated from the relative contribution of the different emitting components in the emission decays of the different composites (Tables S2 and S3). Because the ICT event is an ultrafast process, the relatively slow homo-ET process should occur in CS states of neighboring C153 molecules.

To gain a deeper insight into the excited-state dynamics of the composites at higher $[C153]_0$ (10^{-4}, 10^{-3} and 10^{-2} M), we studied their time-resolved emission behavior. The recorded decays can be grouped into two families: (I) for the bluest region (490–530 nm) and (II) for the reddest one (560–630 nm). The decays global fit in region I gives time constants of 0.26, 2.0, and 5.6 ns for the 10^{-4} M $[C153]_0$ composite; 0.24, 1.5 and 4.5 ns for the 10^{-3} M $[C153]_0$ composite and 0.15, 1.1 and 3.4 ns for the 10^{-2} M $[C153]_0$ composite (Fig. 1, panels D to F and Table 1B and Table S3). For region II, we obtained time

Table 1 Values of the time constants of the emission lifetimes (τ_i), normalized (to 100) pre-exponential factors (A_i) and contribution (C_i) obtained from the multiexponential fit of the emission decays of C153@Al-ITQ-HB with (A) 10^{-5} M $[C153]_0$ and (B) 10^{-3} M $[C153]_0$ observed at different emission wavelengths upon 433 nm excitation

(A) 10^{-5} M $[C153]_0$										(B) 10^{-3} M $[C153]_0$								
λ_{obs} (nm)	τ_1 (ns)	A_1 (%)	C_1 (%)	τ_2 (ns)	A_2 (%)	C_2 (%)	τ_3 (ns)	A_3 (%)	C_3 (%)	τ_1 (ns)	A_1 (%)	C_1 (%)	τ_2 (ns)	A_2 (%)	C_2 (%)	τ_3 (ns)	A_3 (%)	C_3 (%)
490	0.3	14	1	2.4	21	13	5.7	65	86	0.24	42	6	1.5	31	27	4.5	27	65
500	0.3	12	1	2.4	16	9	5.7	72	90	0.24	35	5	1.5	30	20	4.5	35	75
510	0.3	10	0.6	2.4	12	7	5.7	78	92.4	0.24	32	6	1.5	28	27	4.5	40	65
520	0.3	8	0.5	2.4	9	4	5.7	83	95.5	0.24	29	4	1.5	26	21	4.5	45	74
530	0.3	6	0.4	2.4	7	3.7	5.7	87	95.9	0.24	20	2	1.5	24	16	4.5	65	81
560	0.3	3	0.2	2.4	4	1.8	5.7	93	98	0.27	−100	−100	1.5	24	10	4.5	76	90
590	0.3	2	0.1	2.4	1	0.6	5.7	97	99.3	0.27	−100	−100	1.5	5	2	4.5	95	98
630	0.3	2	0.1	2.4	2	0.9	5.7	96	99	0.27	−100	−100	1.5	2	1	4.5	98	99

constants of 0.4 (rise), 2.0 and 5.6 ns for the 10^{-4} M $[C153]_0$ composite; 0.27 (rise), 1.5 and 4.5 ns for the 10^{-3} M $[C153]_0$ composite and 0.2 (rise), 1.1 and 3.4 ns for the 10^{-2} M $[C153]_0$ one (Fig. 1D–F and Table 1B, Table S3). It is worth noting that the shortest component appears as a decay in the bluest region and as a rise in the reddest one, reflecting a common channel that we ascribe to the dynamics of a homo-ET process between neighboring adsorbed C153 molecules. Because the ICT event is an ultrafast process, we suggest that the slower homo-ET occurs in aggregated CS molecules that have suffered this process (Scheme 2). The short time in the bluest region (0.15–0.26 ns) differs from those found in the reddest one (0.20–0.40 ns) due to the short emitting LE species in the former region. The 1.1–2.0 ns and 3.4–5.6 ns are assigned to the lifetimes of the CS species and homo-ET like-aggregate emitters, respectively. At a high $[C153]_0$, the formation of H-aggregates becomes significant, due to strong dipole–dipole and π–π stacking interactions among surface-adsorbed C153. Scheme 2 illustrates the key photophysical processes involved in the electronically first excited state of C153@Al-ITQ-HB composites of three emitters, LE, CS and J-aggregates, connected by ICT and homo-ET events.

3.3. Coumarin 153/Nile Red@Al-ITQ-HB MOF (mixed composites) steady-state photobehaviour

Next, we studied the spectroscopy and photodynamics of the different C153/NR@Al-ITQ-HB composites (solid state). To this end, we synthesized six composites using combinations of three initial concentrations of $[C153]_0$ (10^{-3}, 10^{-4} and 10^{-5} M) and two initial concentrations of $[NR]_0$ (10^{-4} and 10^{-5} M). We looked for the best dyes combination to get more efficient hetero-ET process from C153 to NR within the formed composites. Fig. S5 illustrates the spectral overlap between the emission spectrum of C153 and the absorption one of NR in the formed composites. Exploring the possibility of ET from excited C153 (donor, D) to NR (acceptor, A) adsorbed molecules, we examined the emission (C153) and absorption (NR) spectral positions. The composite formed by 10^{-3} M $[C153]_0$ and 10^{-4} M $[NR]_0$, exhibits the highest spectral overlap between the A and D molecules, while those using 10^{-5} M for both C153 and NR exhibit the lowest spectral overlap. To make the discussion easy, the mixed composites are categorized into two groups: Group 1 ($[NR]_0 = 10^{-4}$ M) and Group 2 ($[NR]_0 = 10^{-5}$ M) with $[C153]_0$ of 10^{-3}, 10^{-4} and 10^{-5} M.

Fig. 2 shows the normalized absorption and emission spectra of the composites. Panels A, B and C exhibit the spectra of Group 1, while panels D, E and F illustrate those of Group 2.

The absorption spectra of Group 1 are primarily dominated by the C153 absorption, whose intensity decreases upon increasing $[C153]_0$. However, the emission ones are dominated by the NR band, indicating efficient hetero-ET from C153 to NR. The absorption of Group 2 shows similar trends as those of Group 1 upon decreasing $[C153]_0$ from 10^{-3} to 10^{-5} M, while the emission ones display bands from both C153 and NR. Note that for Group 2, we also observe a relative decrease in NR emission intensity upon decreasing $[C153]_0$ from 10^{-3} to 10^{-5} M. This could be due to less efficient hetero-ET from C153 to NR. Fig. S6 displays the absorption, emission, and excitation spectra for all the composites, recorded at ∼ 525 nm (emission maximum of C153), and at ∼650 nm (emission maximum intensity of NR). The excitation spectra collected at 525 exhibits a single band, which aligns with the absorption of C153 in the composite. However, the excitation spectra recorded at 650 nm,

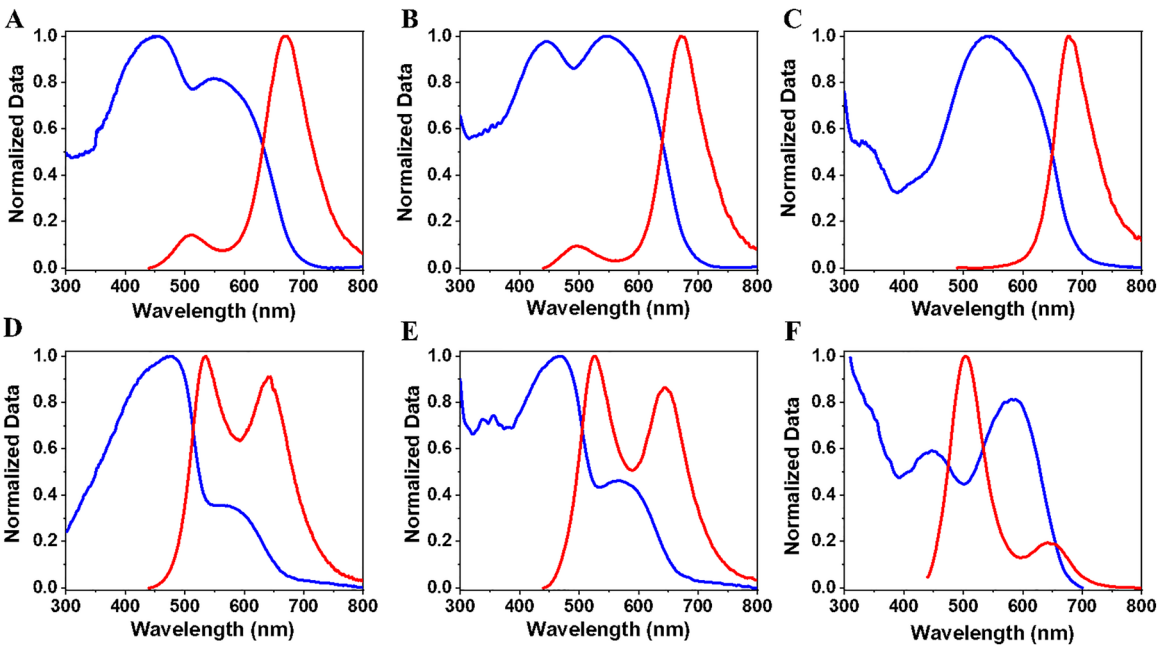

Fig. 2 UV-Vis diffuse reflectance (blue) and emission (red) spectra of the C153/NR@Al-ITQ-HB composites. The excitation wavelength was 425 nm. First row, Group 1 composites: (A) [C153/NR: 10^{-3} M/10^{-4} M]$_0$; (B) [C153/NR: 10^{-4} M/10^{-4} M]$_0$ and (C) [C153/NR: 10^{-5} M/10^{-4} M]$_0$. Second row, Group 2 composites, (D) [C153/NR: 10^{-3} M/10^{-5} M]$_0$; (E) [C153/NR: 10^{-4} M/10^{-5} M]$_0$ and (F) [C153/NR: 10^{-5} M/10^{-5} M]$_0$.

show two bands corresponding to the absorption of both C153 (energy D) and NR (energy A). This clearly confirms the presence of hetero-ET from C153 to NR in the mixed composites. To quantify the ET efficiency between Groups 1 and 2, we calculated its quantum yield (QY) for [C153]/[NR]:10^{-4} M/10^{-4} M of Group 1 and [C153]/[NR]:10^{-4} M/10^{-5} M] of Group 2 (see details in the SI). We obtained an efficiency of 97% for the former and 57% for the latter. The observed difference might be due a change in the distances of the D and A partners in the two mixed composites, as supported by the obtained time constants of this process (*vide infra*).

3.4. Picosecond time-resolved behavior of coumarin 153/Nile Red@Al-ITQ-HB MOF composites

To further characterize the ET process in the mixed composites at different concentrations of both dyes, we conducted TCSPC experiments. We excited the mixed composites at 433 nm (C153 main absorption, energy D) and monitored the emission decays at various wavelengths (490 to 680 nm). Fig. 3 shows the recorded decays. For clarity, the discussion first focuses on Group 1. The photoluminescence lifetimes were analyzed at two spectral regions: blue (490–590 nm, energy D emission) and red (630–680 nm, energy A emission) regions.

Group 1 mixed composites. Panels A and B of Fig. 3 show the emission decays of Group 1 composites, [C153/NR: 10^{-3} M/10^{-4} M]$_0$ and [C153/NR: 10^{-4} M/10^{-4} M]$_0$, and Table 2 presents the obtained data from the best multiexponential fits. In the bluest region, we obtained three time constants: 0.2, 1.1, 3.2 ns, and 0.24, 1.5, 3.7 ns for the [C153/NR: 10^{-3} M/10^{-4} M]$_0$ and [C153/NR: 10^{-4} M/10^{-4} M]$_0$ composites, respectively. The contributions of the three components show similar trends for both composites. In the bluest region, the contributions of the short and intermediate components decrease upon increasing the observation wavelength. The decays in the reddest region display time constants of 0.25 (rise), 1.1 (rise) 4.6 ns, and 0.3 ns (rise), 1.5 ns (rise), and 4.6 ns for [C153/NR: 10^{-3} M/10^{-4} M]$_0$ composite and [C153/NR: 10^{-4} M/10^{-4} M]$_0$ composites, respectively.

The short and intermediate components are decaying in the bluest region and rising in the reddest one. The short component in the decays of both composites shows a trend like the one observed for the 10^{-4} and 10^{-3} M [C153]$_0$ composites, respectively (Table S3A and Table 1A). Therefore, we assign this sub-nanosecond component in the bluest region to the mixed emission decays from the LE and the homo-ET process (~0.2 ns) in adsorbed C153. The corresponding rise in the red region is due to the homo-ET (~0.25 ns) between neighboring C153 molecules (aggregates). On the other hand, the intermediate component (1.1 and 1.5 ns) in the decays of the mixed composites (decay and rise) behaves differently from the one

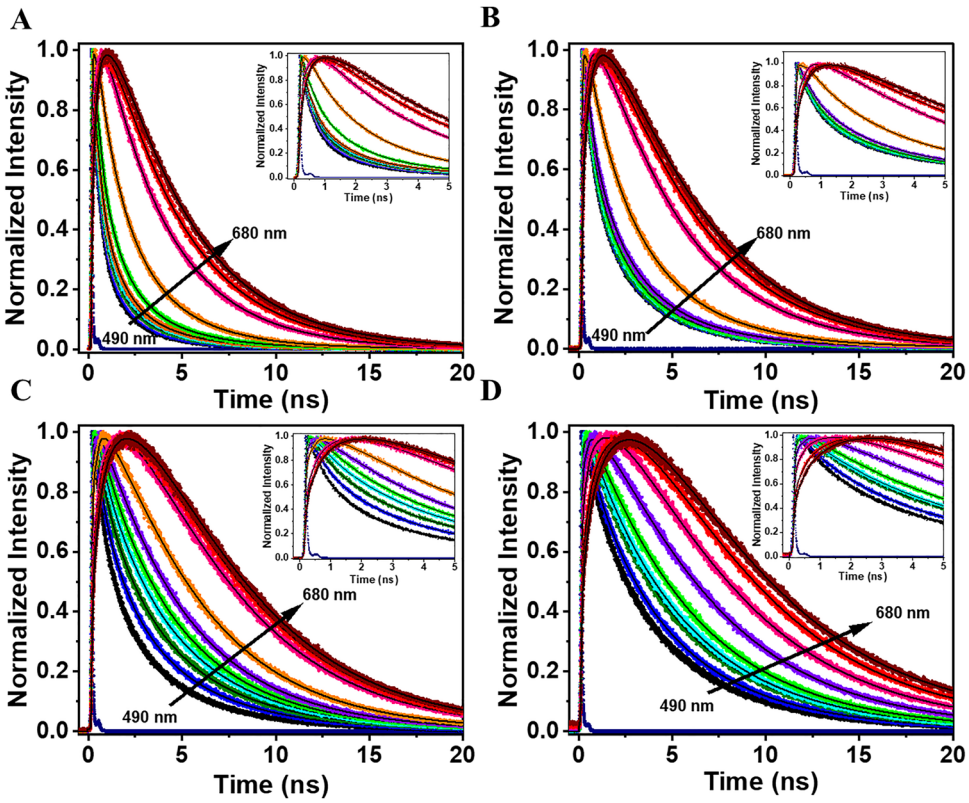

Fig. 3 Emission decays (solid circles) of NR/C153@Al-ITQ-HB composites (linear plots) collected at discrete wavelengths (490, 500, 510, 520, 530, 560, 590, 630, 650 and 680 nm) upon excitation at 433 nm. The solid lines (black) are the multiexponential fits of the decays. The dotted line is the instrument response function (IRF ~ 70 ps; violet). The inset shows the decays plot up to 5 ns. (A) [C153/NR: 10^{-3} M/10^{-4} M]$_0$; (B) [C153/NR: 10^{-4} M/10^{-4} M]$_0$; (C) [C153/NR: 10^{-3} M/10^{-5} M]$_0$; and (D) [C153/NR: 10^{-4} M/10^{-5} M]$_0$.

Table 2 Values of the time constants of the emission lifetimes (τ_i), normalized (to 100) pre-exponential factors (A_i) and contribution (C_i) of the Group 1 mixed composites obtained by multiexponential fit of different emission wavelengths upon 433 nm excitation

[C153/NR: 10^{-3} M/10^{-4} M]										[C153/NR: 10^{-4} M/10^{-4} M]								
λ_{obs} (nm)	τ_1 (ns)	A_1 (%)	C_1 (%)	τ_2 (ns)	A_2 (%)	C_2 (%)	τ_3 (ns)	A_3 (%)	C_3 (%)	τ_1 (ns)	A_1 (%)	C_1 (%)	τ_2 (ns)	A_2 (%)	C_2 (%)	τ_3 (ns)	A_3 (%)	C_3 (%)
490	0.2	59	16	1.1	31	42	3.2	10	42	0.24	40	9	1.5	36	31	3.7	24	60
500	0.2	55	14	1.1	32	41	3.2	12	45	0.24	39	8	1.5	35	30	3.7	26	66
510	0.2	54	13	1.1	33	40	3.2	13	47	0.24	37	6	1.5	34	29	3.7	29	67
520	0.2	52	12	1.1	34	39	3.2	14	49	0.24	36	5	1.5	33	27	3.7	31	68
530	0.2	50	11	1.1	35	38	3.2	15	51	0.24	35	4	1.5	32	26	3.7	33	70
560	0.2	39	8.2	1.1	41	38	3.2	20	53	0.24	31	3	1.5	30	24	3.7	39	73
590	0.2	8.7	1.3	1.1	50	34	3.2	41	65	0.24	8	1	1.5	28	16	3.7	64	83
630	0.25	−47	−47	1.1	−53	−53	4.6	100	100	0.30	−54	−54	1.5	−46	−46	4.6	100	100
650	0.25	−48	−48	1.1	−52	−52	4.6	100	100	0.30	−36	−36	1.5	−64	−64	4.6	100	100
680	0.25	−52	−52	1.1	−48	−48	4.6	100	100	0.30	−33	−33	1.5	−67	−67	4.6	100	100

found in the single dye composites signals (only decay). We assign this intermediate component to hetero-ET dynamics from C153 to NR, both adsorbed on Al-ITQ-HB MOF surface. Finally, the time constant of the longest ns-component that is present as a decay through all the spectral range of observation increases its value with the monitored wavelength, being 3.3–3.7 ns at the bluest region, and 4.6 ns at the reddest one. This behavior suggests different species that emit in these regions, in agreement with the nature of the mixed composites containing C153 (blue emitter) and NR (red emitter), and their emission spectra (Fig. 2A and B). Hence, we assign the time component obtained in the bluest region to a population of C153 (most probably J-aggregates in combination with emission from CS state) undergoing an ET process, while the one in the reddest region corresponds to the emission lifetime of NR molecules that receives energy from excited C153 ones. The value of the long-time component (3.2 ns and 3.7 ns) of C153 in the mixed composites is shorter than the one corresponding to the emission from the J-aggregates of the 10^{-3} M (4.5 ns) and 10^{-4} M (5.6 ns) $[C153]_0$ single-dye composites, reflecting the occurrence of ET from the population of the C153 to NR. In these mixed composites, the time constant of homo-ET process ($\sim$ 0.25 ns) is shorter than the hetero-ET (1.1–1.5 ns) one. However, the latter is remarkably slower than the reported one on C153 and NR encapsulated within PVK polymer nanoparticles (70 ps).[50] The difference in the time of the hetero-ET process in these materials could be attributed to the layered structure of Al-ITQ-HB, which may result in a greater distance and less favorable orientation between the D and A dyes adsorbed on Al-ITQ-HB, and the possibility of confining C153 and NR molecules within the same space of the polymer, shortening the ET time in the latter. On the other hand, we have reported that encapsulated C153 and NR molecules within a 3D Zr-based MOF did not show a hetero-ET and explained it in terms of their locations in cavities not allowing adequate orientations for ET or having a longer A–D distance.[36] In the present composites, using a layered 2D-MOF, the hetero-ET between both dyes is efficient and happens in the ns regime.

To further understand the emission behavior of Group 1, we selectively excited NR in the mixed composites at 505 nm and compared the results with those of the single NR composites prepared with the same initial dye concentration 10^{-4} M $[NR]_0$. Fig. S7, panel A and B, and Fig. S8A show the emission decays, gated at discrete wavelengths (560 to 730 nm). The short and intermediate components behave as decays in the greenest region (560 to 610 nm) and rise in the reddest one (630 to 730 nm), while the long-time components behave as decay over all the monitored wavelengths (Tables S4A, B and S5A). This behavior is consistent with the decay observed of the 10^{-4} M $[NR]_0$ composites excited at 505 nm (Fig. S9A and Table S6A), confirming that the observed emission upon excitation at 505 nm of the mixed systems originates primarily from NR, and follows a similar photophysical pathway. In agreement with previous reports on the interaction of NR with Al-ITQ-HB, we assign the short and intermediate components to homo-ET between NR molecules.[44,46,47] These fast processes likely reflect homo-ET among closely packed NR molecules adsorbed on the polar domains of the MOF, which facilitates redistribution of the excitation energy before decaying to the ground state. The rise observed in the red region further supports this assignment. The long-lived component ($\sim$4 ns), on the other hand, corresponds to emission from a photoinduced CT state of NR.[44,46,47,51] Thus, Group 1 shows direct emission from adsorbed NR or through ET from adsorbed C153 molecules.

Group 2 mixed composites. Fig. 3C and D exhibit the decays of Group 2, [C153/NR: 10^{-3} M/10^{-5} M]$_0$ and [C153/NR: 10^{-4} M/10^{-5} M]$_0$ at different wavelengths of observation upon excitation at 433 nm. In the bluest region, the analysis gives: 0.33, 2.2, and 4.7 ns for [C153/NR: 10^{-3} M/10^{-5} M]$_0$; 0.35, 2.5 and 5.3 ns for [C153/NR: 10^{-4} M/10^{-5} M]$_0$ (Table 3). In the reddest region, we also obtained three time constants: 0.36 ns (rise), 2.2 ns (rise), and 5.3 ns for [C153/NR:10^{-3} M/10^{-5} M]$_0$; 0.40 ns (rise), 2.5 ns (rise), and 6.5 ns for [C153/NR: 10^{-4} M/10^{-5} M]$_0$.

The short time component that is present as a decay in the bluest region and as a rise in the reddest one for both composites has similar values and shows comparable behaviour as those found for both the single C153 composites (10^{-3} and 10^{-4} M $[C153]_0$) and the mixed dye composites in Group 1. Therefore, we assign it to a combined contribution from the LE state emission and homo-ET in the bluest region, and to the homo-ET in the reddest one. The intermediate component

Table 3 Values of the emission lifetimes (τ_i) normalized (to 100) pre-exponential factors (A_i) and contribution (C_i) of the Group 2 mixed composites obtained by multiexponential fit of different emission wavelengths upon 433 nm excitation

	[C153/NR: 10^{-3} M/10^{-5} M]										[C153/NR: 10^{-4} M/10^{-5} M]								
λ_{obs} (nm)	τ_1 (ns)	A_1 (%)	C_1 (%)	τ_2 (ns)	A_2 (%)	C_2 (%)	τ_3 (ns)	A_3 (%)	C_3 (%)		τ_1 (ns)	A_1 (%)	C_1 (%)	τ_2 (ns)	A_2 (%)	C_2 (%)	τ_3 (ns)	A_3 (%)	C_3 (%)
490	0.33	39	11	2.2	35	34	4.7	24	55		0.35	17	10	2.5	35	23	5.3	48	67
500	0.33	29	10	2.2	33	25	4.7	37	65		0.35	14	9	2.5	25	15	5.3	61	76
510	0.33	21	7	2.2	27	17	4.7	52	76		0.35	10	8	2.5	13	12	5.3	77	80
520	0.33	12	6	2.2	20	11	4.7	66	83		0.35	8	7	2.5	11	10	5.3	81	83
530	0.33	6	4	2.2	15	7	4.7	78	89		0.35	6	5	2.5	9	8	5.3	85	87
560	0.33	4	2	2.2	5	3	4.7	91	95		0.35	5	3	2.5	8	7	5.3	87	90
590	0.33	2	1	2.2	3	2	4.7	95	97		0.35	2	1	2.5	4	3	5.3	94	96
630	0.36	−27	−27	2.2	−63	−63	5.3	100	100		0.40	−12	−12	2.5	−88	−88	6.5	100	100
650	0.36	−20	−20	2.2	−80	−80	5.3	100	100		0.40	−10	−10	2.5	−90	−90	6.5	100	100
680	0.36	−18	−18	2.2	−88	−88	5.3	100	100		0.40	−10	−10	2.5	−90	−90	6.5	100	100

(2.2 and 2.5 ns), present as a decay in the bluest region and as a rise in the reddest one, is attributed to the hetero-ET from excited C153 to NR molecules. The time constant is longer than the one in Group 1 (1.1 ns), which is explained in terms of a longer distance between D and A dyes due to the tenfold lower population of NR molecules (10^{-5} M $[NR]_0$). We assign the long decay components in the bluest region (4.7 and 5.3 ns) to the emission from CS and J-aggregates of C153. As discussed for the Group 1 composites behavior, hetero-ET occurs from a C153 with mostly J-aggregate character to NR molecules. It is worth noting that despite Group 2 composites having the same initial concentrations of C153 as in Group 1, their decays exhibit longer J-aggregate emission lifetimes (4.7 and 5.3 ns), when compared to Group 1 (3.2 and 3.7 ns), which suggests a reduced hetero-ET process from J-aggregates of C53 to NR in Group 2. Moreover, the J-aggregate lifetimes in this group are comparable to those in the C153 composites (4.5 ns for 10^{-3} and 5.6 ns for 10^{-4} M $[C153]_0$). Therefore, we suggest that, in the Group 2 composites, the hetero-ET predominantly occurs from a C153 population with CS character.

Finally, the long-time components in the red-emission region of Group 2 (5.3 ns for [C153/NR: 10^{-3} M/10^{-5} M]$_0$ and 6.5 ns for [C153/NR: 10^{-4} M/10^{-5} M]$_0$) are attributed to emission from NR monomers. These values are larger than the corresponding ones obtained in Group 1 and the 10^{-5} M $[NR]_0$ composite.[46] We explain the increase in the corresponding value for the NR monomer in the Group 2 composites in terms of a reduced NR concentration, which on one hand favours the monomers population over the aggregates one, and on the other, the access to the nonpolar environment of Al-ITQ-HB.[52]

To further understand the emission of Group 2, we also recorded their decays at different wavelengths (560–730 nm) upon selective excitation of NR at 505 nm (Fig. S7C, D and S8B). The best fits give time constants of 0.5, 2.4 and 4.8 ns for [C153/NR: 10^{-3} M/10^{-5} M] composite; 0.45, 2.2 s and 4.8 ns for [C153/NR: 10^{-4} M/10^{-5} M] one; and 0.3, 2.4 and 4.6 ns for [C153/NR: 10^{-5} M/10^{-5} M] one (Tables S5B and S7A, B). Due to the nature of the Group 2 composites, it is expected that they should show comparable time components as of 10^{-5} M $[NR]_0$ composites excited at 505 nm (Fig. S9B and Table S6B). Indeed, the intermediate and long components show similar relative contribution trends to those observed for the 10^{-5} M $[NR]_0$ composites excited at 505 nm. Therefore, we assign the intermediate component to homo-ET between NR molecules and the long component to emission from the CS state of NR.[46,47,51] However, unlike the 10^{-5} M $[NR]_0$ composite, the Group 2 composites show a short component in both the green (as decay) and red (as rise) regions. This decay and rise behaviour indicate a common channel, which we assign to the presence of homo-ET process between NR molecules. Interestingly, the presence of C153 in these composites influences the homo-ET of NR, possibly by altering its spatial organization, distance or local environment within the composite matrix.

Scheme 3 summarizes the key photophysical processes occurring in the mixed-dye composites [C153/NR@Al-ITQ-HB]. Upon excitation of C153 to the first electronically excited state, two ET pathways are possible: homo-ET between C153 molecules and hetero-ET from C153 to NR, resulting in a dual green and emission. Direct excitation of NR leads to homo-ET process between NR molecules emitting in the red region. Notably, depending on the NR initial concentration, the ET from C153 can be more (Group 1) or less (Group 2) efficient.

3.5. Single crystal photobehavior of mixed composites and their CIE chromaticity

To further characterize the distributions of the D and A and their effects on the ET process in the mixed composites, we performed fluorescence lifetime imaging (FLIM) of C153/NR@Al-ITQ-HB ([C153/NR: 10^{-4} M/10^{-4} M]$_0$) crystals (C1–C3) under the microscope. The single crystals were excited at 390 nm and the FLIM images were collected in two spectral regions corresponding to the donor (C153, 475–525 nm) and to the acceptor (NR, 650–740 nm) emissions. Fig. 4 (panels A to D) shows representative FLIM images of 3 crystals and the corresponding emission decays. On one hand, the FLIM images show homogeneous distribution of the emitting species both in the D (Detector 1, C153) and A (Detector 2, NR) spectral regions within each crystal and on the other, they present different loading ratios of the D and A molecules. The difference in the loading is reflected also in the average dynamical behaviour of each of the crystals (Table 4). The average emission decay for crystal 1 (C1) presents a profile comparable to the ensemble

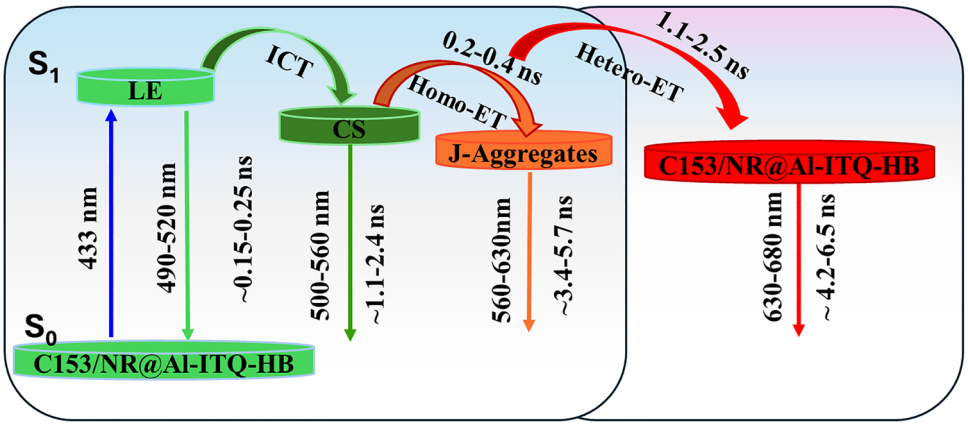

Scheme 3 Photophysical processes (not to scale) and the corresponding lifetime values giving information of spectral and dynamical behavior upon excitation of C153 in C153/NR@Al-ITQ-HB composites. LE, ICT, CS and ET stand for locally excited state, intramolecular charge transfer, charge-separated state and energy transfer, respectively. Spectral ranges are estimated from the relative contribution of the different emitting components in the decays of the different composites (Tables 1, 2 and Tables S2, S3). Note that the hetero-ET can occur from either CS or J-aggregates or a combination of both depending on the acceptor (NR) concentration.

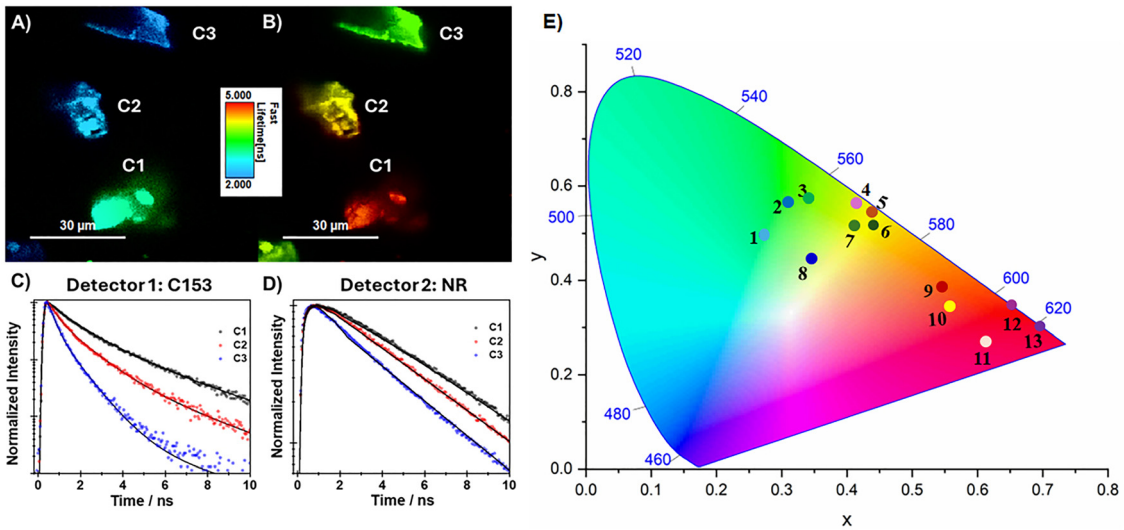

Fig. 4 FLIM images for representative crystals (C1, C2 and C3) of the [C153/NR: 10^{-4} M/10^{-4} M] mixed composite collected at (A) Detector 1 (C153 emission, 475–525 nm) and (B) Detector 2 (NR emission, 650–740 nm). Representative average emission transient for the crystals (C1, C2 and C3) in (A) and (B), collected at (C) Detector 1 (C153 emission, 475–525 nm) and (D) Detector 2 (NR emission, 650–740 nm). The excitation wavelength was 390 nm; (E) The CIE chromaticity coordinates of the C153@Al-ITQ-HB, [C153/NR@Al-ITQ-HB] and NR@Al-ITQ-HB. ((1) 10^{-6} M $[C153]_0$, (2) 10^{-5} M $[C153]_0$, (3) 10^{-4} M $[C153]_0$, (4) 10^{-3} M $[C153]_0$, (5) 10^{-2} M $[C153]_0$, (6) [C153/NR: 10^{-3} M/10^{-5} M]$_0$, (7) [C153/NR: 10^{-4} M/10^{-5} M]$_0$, (8) [C153/NR: 10^{-5} M/10^{-5} M]$_0$, (9) [C153/NR: 10^{-3} M/10^{-4} M]$_0$, (10) [C153/NR: 10^{-4} M/10^{-4} M]$_0$, (11) [C153/NR: 10^{-5} M/10^{-4} M]$_0$, (12) 10^{-5} M $[NR]_0$, (13) 10^{-4} M $[NR]_0$).

average ones for the same composite. The multiexponential fit of the decay collected at the donor channel gives three-time components of 0.32 ns (20%), 1.4 ns (50%) and 3.5 ns (30%), while that at the acceptor one we obtained only two components with times of 1.5 and 4.6 ns. The 1.5-ns component is present as a rise. These values are comparable to those observed for the ensemble average mixed composites. Hence, we interpret the observed photodynamical behaviour analogously – the 0.32 decay component observed only in the decay at Detector 1 corresponds to the LE/H-aggregate/homo-ET of the excited C153, while the 1.4–1.5 ns decay and rise component corresponds to the hetero-ET from C153 to NR. The long-time components, 3.5 ns (D1) and 4.6 ns (D2), correspond to the emission lifetimes of the CS/J-aggregate populations of C153 and ET-excited NR, respectively.

It should be noted that contrary to the ensemble average results, we did not observe the rising component associated with the homo-ET of C153 (0.32 ns) in the decay collected at Detector 2 most probably due to the longer time-resolution of the microscope (~0.26 ns). The behaviour of the emission transients of C2 collected at both detectors follows a similar trend to that of C1, with the notable exception of the component assigned to the ET process, which has a lower value for the case of C2 (1.2 ns). Since at 390 nm we are exciting

Table 4 Values of the time constants (τ_i) and normalized (to 100) pre-exponential factors (a_i) obtained from the fit of the emission decays for three different crystals (C1, C2 and C3) of the [C153/NR: 10^{-4} M/10^{-4} M]$_0$ mixed composite shown in Fig. 4(A–D). The negative sign (–) indicates rising component

	Detector 1 (C153, 475–525 nm)						Detector 2 (NR, 650–740 nm)			
Sample	τ_1/ns	a_1	τ_2/ns	a_2	τ_3/ns	a_3	τ_1/ns	a_1	τ_2/ns	a_2
C1	0.32	20	1.4	50	3.5	30	1.5	(–)100	4.6	100
C2	0.34	30	1.2	40	3.2	30	1.2	(–)100	4.5	100
C3	0.30	70	—	—	3.2	30	—	—	4.2	100

predominantly C153, this decrease can be explained with the possible higher loading of C153 in C2 that can give rise to faster ET due to a shortening in the distance between the D and A molecules in the composites.

This interpretation is further supported by the average emission decays of C3. While we still see the decay of the ET-produced NR emission, no indication of rising component is observed, and the emission transient decays monoexponentially with a time constant of 4.2 ns. On the other hand, the emission signal of C3 at Detector 1 decays biexponentially with time constant of 0.3 and 3.2 ns corresponding the emission of C153. These results indicate that while the ensemble average studies present a global vision for the behaviour of each composite, for these samples, one needs to consider both the individual loadings of the D and A dyes in the crystals, as well as the inter-crystal interactions.

To finalize this subsection, Fig. 4E shows, through the CIE coordinates chromaticity diagram, the tunable emission colors achieved by varying the concentrations of C153 and NR in the studied composites. Each point on the diagram corresponds to the chromaticity coordinates of a specific dye mixture at Al-ITQ-HB, with pure C153 samples clustering in the blue-green region and mixtures with increasing NR content shifting toward yellow, orange, and red emissions. This progression visually demonstrates efficient ET from C153 to NR, allowing gradual control over the emission of the composite across the visible spectrum, a feature valuable for applications in optoelectronics and color-tunable devices. The emission closest to WL was obtained from [C153/NR: 10^{-4} M/10^{-5} M]$_0$, and the coordinates of this point in the CIE plot are x = 0.41 and y = 0.51.

4. Conclusion

To develop an efficient ET system for dual emission, we investigated the photophysical behavior of individual and mixed dye composites interacting with Al-ITQ-HB 2D MOF. First, we studied the effect of the initial concentration of C153 on the photophysical properties of the formed single dye-MOF matrix composites. The C153@Al-ITQ-HB composite exhibits two distinct monomer emission states linked to its interaction with different domains of Al-ITQ-HB: a locally excited (LE) state (~0.3 ns) and a charge-separated (~2.4 ns) one, along with emission from J-aggregates (~5.7 ns). Increasing C153 concentration promotes H-aggregates formation, leading to pronounced emission quenching caused by strong dipole–dipole interactions.

Next, we studied binary C153/NR@Al-ITQ-HB mixed composites varying the initial concentration of the two dyes to characterize the hetero-ET efficiency and donor–acceptor interplay, identifying optimal conditions for either dominant ET or balanced dual emission. For these composites, changes in NR concentration give rise to markedly different photophysical behaviors. Group 1 composites (with 10^{-4} M [NR]$_0$) exhibit a dominant emission peak corresponding to NR and highly efficient hetero-energy transfer (ET), mainly originating from a C153 J-aggregates population to NR adsorbed molecules on the MOF. The Group 2 composites (with 10^{-5} M [NR]$_0$) exhibit emission from both dyes, but with reduced ET efficiency due to a lower acceptor population, with ET mainly occurring from a C153 population with predominantly CS character. The observed hetero-ET time constant for Group 1 composites is 1.1 ns, while for those in Group 2 it is 2.5 ns. Fluorescence lifetime imaging microscopy (FLIM) further elucidated that spatial heterogeneity of donor and acceptor molecules between crystals of the same sample also affects the ET kinetics. We conclude that Group 1 composites are best suited for efficient ET, whereas Group 2 composites hold greater potential for potential white light generation in combination with blue emitters.

These findings highlight the critical influence of dye concentration, aggregation behavior, inter-crystal dye loading, and MOF structure on ET efficiency and emission performance. The strategic integration of donor–acceptor pairs within the Al-ITQ-HB scaffold provides a robust and modular platform for the rational design of luminescent composites for possible optoelectronic applications.

Author contributions

U. Diaz and J. Torró-Abril synthesized and characterized the Al-ITQ-HB 2D MOFs. S. Mishra, B. Cohen and A. Douhal, synthesized, performed the related experiments, analyzed, and discussed the spectroscopic characterization of the composites. B. Cohen and A. Douhal designed, supervised, and discussed the experimental work. All authors contributed to the manuscript writing and discussed the results.

Conflicts of interest

The authors declare no conflict of interest.

Data availability

The data that support the findings of this study are available from the corresponding authors upon reasonable request.

Supplementary information (SI): materials and synthesis method of Al-ITQ-HB, C153 composites, C153/NR mixed composites. Morphological characteristics of Al-ITQ-HB, C153@Al-ITQ-HB and [C153/NR@Al-ITQ-HB] material from TEM

analysis. Images of C153 composites and mixed composites under day light and UV light. Comparative UV-vis absorption, emission spectra of C153 composites of different initial concentrations and C153 dye in solid states. UV-vis absorption, emission, and excitation spectra of each C153 composite. TCSPC decay plots (10^{-6} M-10^{-2} M) (up to 20 ns) and Table for time components with their contribution (10^{-4}, 10^{-5} and 10^{-6} M), upon excitation at 433 nm and monitored at different wavelengths of C153 composites. Compared absorption, emission spectra of C153 and NR composites for different initial concentration. Absorption, emission, and excitation spectra of mixed composites. Calculation of energy transfer efficiency from C153 to NR. Decay plot of NR composites after excitation at 505 nm. Time components with their contribution of NR composites and mixed composites after excitation at 505 nm and monitored at different wavelengths. See DOI: https://doi.org/10.1039/d5tc04261e.

Acknowledgements

This work was supported by the following projects: PID2020-116519RB-I00 and TED2021-131650B–I00 funded by MICIU/AEI/10.13039/501100011033 and the European Union (EU), and SBPLY/23/180225/000196 funded by JCCM and the EU through ''Fondo Europeo de Desarrollo Regional'' (FEDER) and 2025-GRIN-38517 funded by UCLM (FEDER). U.D. and J.T. are grateful for the financial support from the Spanish Ministry (projects PID2023-146114NB-C21, PRE2021-098576 and CEX2021-001230-S, funded by MCIN/AEI/10.13039/501100011033) and from the Advanced Materials program, supported by MCIN with funding from the European Union NextGeneration (PRTRC17.I1) and by Generalitat Valenciana (MFA/2022/003).

References

1 A. S. Sadhu, Y.-M. Huang, L.-Y. Chen, H.-C. Kuo and C.-C. Lin, *Nanomaterials*, 2022, **12**(6), 985.
2 S. Rakshit, P. Piatkowski, I. Mora-Seró and A. Douhal, *Adv. Opt. Mater.*, 2022, **10**(14), 2102566.
3 E. F. Schubert and J. K. Kim, *Science*, 2005, **308**(5726), 1274.
4 S. V. Eliseeva and J.-C. G. Bünzli, *Chem. Soc. Rev.*, 2010, **39**(1), 189.
5 B. Fitzhenry, *Appl. Opt.*, 1979, **18**(19), 3332.
6 D. Citterio, L. Jenny, S. Rásonyi and U. E. Spichiger, *Sens. Actuators, B*, 1997, **39**(1–3), 202.
7 J. Bhattacharjee, S. Mishra and A. P. Das, *Appl. Biochem. Biotechnol.*, 2022, **194**(10), 4745.
8 Z. Yang, J. Cao, Y. He, J. H. Yang, T. Kim, X. Peng and J. S. Kim, *Chem. Soc. Rev.*, 2014, **43**(13), 4563.
9 A. C. Grimsdale, K. Leok Chan, R. E. Martin, P. G. Jokisz and A. B. Holmes, *Chem. Rev.*, 2009, **109**(3), 897.
10 C.-H. Chen, P.-T. Chou, T.-C. Yin, K.-F. Chen, M.-L. Jiang, Y. J. Chang, C.-K. Tai and B.-C. Wang, *Org. Electron.*, 2018, **59**, 69.
11 N. Mariotti, M. Bonomo, L. Fagiolari, N. Barbero, C. Gerbaldi, F. Bella and C. Barolo, *Green Chem.*, 2020, **22**(21), 7168.
12 C. Ji, L. Lai, P. Li, Z. Wu, W. Cheng and M. Yin, *Aggregate*, 2021, **2**(4), e39.
13 F. Würthner, *Angew. Chem., Int. Ed.*, 2020, **59**(34), 14192.
14 F. Xu, T. T. Testoff, L. Wang and X. Zhou, *Molecules*, 2020, **25**(19), 4478.
15 M. K. Bera, P. Pal and S. Malik, *J. Mater. Chem. C*, 2020, **8**(3), 788.
16 E. Arunkumar, C. C. Forbes and B. D. Smith, *Eur. J. Org. Chem.*, 2005, (19), 4051.
17 C. Martin, M. Rosaria di Nunzio, B. Cohen and A. Douhal, *Photochem. Photobiol. Sci.*, 2014, **13**, 1580.
18 W. Arfi, A. Khan, F. Moulai, K. Agroui, C. Baretta, G. Oreski and M. Jaunich, New Concepts in Solar and Thermal Radiation Conversion and Reliability SPIE, 2018, 71–79.
19 L. J. Murray, M. Dincă and J. R. Long, Hydrogen Storage in Metal-Organic Frameworks, *Chem. Soc. Rev.*, 2009, **38**, 1294.
20 M. Pan, X.-M. Lin, G.-B. Li and C.-Y. Su, *Coord. Chem. Rev.*, 2011, **255**(15–16), 1921.
21 X. L. Wang, C. Qin, S. X. Wu, K. Z. Shao, Y. Q. Lan, S. Wang, D. X. Zhu, Z. M. Su and E. B. Wang, *Angew. Chem.*, 2009, **121**(29), 5395.
22 C.-Y. Sun, C. Qin, C.-G. Wang, Z.-M. Su, S. Wang, X.-L. Wang, G.-S. Yang, K.-Z. Shao, Y.-Q. Lan and E.-B. Wang, *Adv. Mater.*, 2011, **23**(47), 5629.
23 G. Lu, S. Li, Z. Guo, O. K. Farha, B. G. Hauser, X. Qi, Y. Wang, X. Wang, S. Han and X. Liu, *Nat. Chem.*, 2012, **4**(4), 310.
24 J. Dong, Z. Qiao, Y. Pan, S. B. Peh, Y. D. Yuan, Y. Wang, L. Zhai, H. Yuan, Y. Cheng and H. Liang, *Chem. Mater.*, 2019, **31**(13), 4897.
25 J. S. Seo, D. Whang, H. Lee, S. I. Jun, J. Oh, Y. J. Jeon and K. Kim, *Nature*, 2000, **404**(6781), 982.
26 Y. Takashima, V. M. Martínez, S. Furukawa, M. Kondo, S. Shimomura, H. Uehara, M. Nakahama, K. Sugimoto and S. Kitagawa, *Nat. Commun.*, 2011, **2**(1), 168.
27 M. R. di Nunzio, E. Caballero-Mancebo, B. Cohen and A. Douhal, *J. Photochem. Photobiol. C: Photochem. Rev.*, 2020, **44**, 100355.
28 M. Gutiérrez, Y. Zhang and J.-C. Tan, *Chem. Rev.*, 2022, **122**(11), 10438.
29 Y. Gai, Q. Guo, K. Xiong, F. Jiang, C. Li, X. Li, Y. Chen, C. Zhu, Q. Huang and R. Yao, *Cryst. Growth Des.*, 2017, **17**(3), 940.
30 Y. Wang, H. Wu, W. Hu and J. F. Stoddart, *Adv. Mater.*, 2022, **34**(22), 2105405.
31 M. D. Allendorf, C. A. Bauer, R. Bhakta and R. Houk, *Chem. Soc. Rev.*, 2009, **38**(5), 1330.
32 Y. Cui, Y. Yue, G. Qian and B. Chen, *Chem. Rev.*, 2012, **112**(2), 1126.
33 J.-X. Wang, J. Yin, O. Shekhah, O. M. Bakr, M. Eddaoudi and O. F. Mohammed, *ACS Appl. Mater. Interfaces*, 2022, **14**(8), 9970.
34 J.-J. Liu, J.-J. Fu, T. Liu, X. Shen and F.-X. Cheng, *Dyes Pigm.*, 2022, **205**, 110542.

35 Z. Wang and C. Wang, *Adv. Mater.*, 2021, **33**(50), 2005819.
36 M. Gutiérrez, F. Sánchez and A. Douhal, *J. Mater. Chem. C*, 2015, **3**(43), 11300.
37 M. Huang, Z. Liang, J. Huang, Y. Wen, Q.-L. Zhu and X. Wu, *ACS Appl. Mater. Interfaces*, 2023, **15**(8), 11131.
38 N. Ahmad, H. A. Younus, A. H. Chughtai, K. Van Hecke, Z. A. Khattak, Z. Gaoke, M. Danish and F. Verpoort, *Catal. Sci. Technol.*, 2018, **8**(16), 4010.
39 X. Hu, Z. Wang, B. Lin, C. Zhang, L. Cao, T. Wang, J. Zhang, C. Wang and W. Lin, *Chem. - Eur. J.*, 2017, **23**(35), 8390.
40 J. M. Moreno, A. Velty, J. A. Vidal-Moya, U. Díaz and A. Corma, *Dalton Trans.*, 2018, **47**(15), 5492.
41 P. García-García, J. M. Moreno, U. Díaz, M. Bruix and A. Corma, *Nat. Commun.*, 2016, **7**(1), 10835.
42 M. Gutiérrez, U. Díaz, B. Cohen and A. Douhal, *J. Mater. Chem. C*, 2023, **11**(41), 14043.
43 M. Choi, K. Na, J. Kim, Y. Sakamoto, O. Terasaki and R. Ryoo, *Nature*, 2009, **461**(7261), 246.
44 E. Caballero-Mancebo, B. Cohen, J. M. Moreno, A. Corma, U. Díaz and A. Douhal, *ACS Omega*, 2018, **3**(2), 1600.
45 M. R. Di Nunzio, M. Gutiérrez, J. M. Moreno, A. Corma, U. Díaz and A. Douhal, *Int. J. Mol. Sci.*, 2021, **23**(1), 330.
46 E. Caballero-Mancebo, J. M. a Moreno, A. Corma, U. Diaz, B. Cohen and A. Douhal, *ACS Appl. Mater. Interfaces*, 2018, **10**(23), 20159.
47 E. Caballero-Mancebo, J. M. Moreno, B. Cohen, U. Díaz, A. Corma and A. Douhal, *ACS Appl. Mater. Interfaces*, 2018, **10**(38), 32885.
48 P. Verma and H. Pal, *J. Phys. Chem. A*, 2014, **118**(34), 6950.
49 J. Liu, C. Chen and C. Fang, *Chemosensors*, 2022, **10**(10), 411.
50 M. Sayed, D. K. Maity and H. Pal, *J. Photochem. Photobiol. A: Chem.*, 2023, **434**, 114265.
51 C. Martin, S. Bhattacharyya, A. Patra and A. Douhal, *Photochem. Photobiol. Sci.*, 2014, **13**, 1241.
52 C. Gajo, D. Shchepanovska, J. F. Jones, G. Karras, P. Malakar, G. M. Greetham, O. A. Hawkins, C. J. Jordan, B. F. Curchod and T. A. Oliver, *J. Phys. Chem. B*, 2024, **128**(47), 11768.

